Chinese Chemical Letters 34 (2023) 107862

Contents lists available at ScienceDirect

Chinese Chemical Letters

journal homepage: www.elsevier.com/locate/cclet

Selective electroreduction of nitrate to ammonia *via* $NbWO_6$ perovskite nanosheets with oxygen vacancy

Tao Feng[a], Fengting Li[b,c], Xiaojun Hu[a,*], Ying Wang[b,c,*]

[a] School of Chemical and Environmental Engineering, Shanghai Institute of Technology, Shanghai 201418, China
[b] State Key Laboratory of Pollution Control and Resources Reuse, College of Environmental Science and Engineering, Tongji University, Shanghai 200092, China
[c] Shanghai Institute of Pollution Control and Ecological Security, Shanghai 200092, China

ARTICLE INFO

Article history:
Received 4 June 2022
Revised 10 September 2022
Accepted 26 September 2022
Available online 28 September 2022

Keywords:
Nitrate reduction
Ammonia generation
$NbWO_{6-x}$ nanosheets
Oxygen vacancy
Adsorption energy

ABSTRACT

Electrocatalytic nitrate reduction to ammonia (NRA) under ambient conditions is significant for carbon-neutral synthetic fuels. Nevertheless, the lack of efficient electrocatalysts with tunable nanostructure for NRA remains a grand challenge. Herein, $NbWO_6$ nanosheets with oxygen vacancy ($NbWO_{6-x}$) was demonstrated *via* thermal treatment and exfoliation with NH_3 selectivity of 86.8% and Faradaic efficiency of 85.7% toward NRA. ^1H nuclear magnetic resonance spectra coupled with ^{15}N isotope labeling experiments proved that NH_3 originated from NO_3^-. The function of oxygen vacancy was revealed by computational studies in NRA. Moreover, the reaction mechanism and pathway of NRA could be deduced based on the results of online differential electrochemical mass spectrometry (DEMS). This work provides a selective NH_3 generation strategy to decarbonize the energy-chemical sector, bridging the gap between batteries and biofuels.

Ammonia (NH_3) as a hydrogen-rich fuel may solve the problem of H_2 transportation and storage [1,2]. Nevertheless, gray NH_3 generation relies great possibility on the century-old Haber-Bosch process leading to a large carbon footprint [3]. Thus, using renewable energy to achieve electrocatalytic green NH_3 synthesis is a promising path [4]. Although N_2 reduction reaction (NRR) process can produce green NH_3, it is relatively energy-intensive due to the high dissociation energy of N≡N bond and low solubility of N_2 in water [5].

Nitrate (NO_3^-) as a highly water-soluble N source requires a lower energy of 204 kJ/mol for breaking N=O bond compared with N≡N bond dissociation [6]. In addition, accumulation of NO_3^- have caused a water pollutant threating to environment and human health [7–10]. Electrocatalytic NO_3^- reduction to NH_3 (NRA) is the most promising path for green NH_3 generation [11,12]. NH_3 can be easily reclaimed from ammonia aqueous solution *via* regenerated resins or air stripping [13]. However, the poor adsorption and activation of NO_3^- ability and complicated eight-electron process as well as the competitive hydrogen evolution reaction (HER) continue to hinder the NRA [14–16]. Therefore, developing efficient and selective electrocatalysts toward NRA that can improve Faradaic efficiency and activate the NO_3^- is urgently needed.

Oxygen vacancies (OVs) are anion vacancy defect that can be used in semiconductor metal oxides. Particularly, tungsten (W) based catalysts with OVs have been widely used to improve the performance of selective NH_3 synthesis. For example, WO_{3-x} nanowires and WO_{3-x} nanosheets with OVs could impact on N species adsorption and suppression of the competing HER to some extent [17]. Therefore, it can be reasonably anticipated that OVs in W-based catalysts can effectively capture N species and reduce it. Recently, W-based perovskite oxides nanosheets with the potential to tune OVs have expected their great potential toward NH_3 synthesis owing to ultrathin thickness, high surface-volume ratio, and various metallic oxide composition [18]. However, studies on W-based perovskite oxides nanosheets containing OVs for NRA have rarely been reported.

Herein, the $NbWO_6$ nanosheets with OVs ($NbWO_{6-x}$) were demonstrated to provide large surface area with fully exposed active interface as well as specific interacting d orbital electrons, which perform high NH_3 selectivity and Faradaic efficiency for NRA. ^{15}N isotope labeling coupled with ^1H nuclear magnetic resonance (^1H NMR) spectra experiments proved that NH_3 originated from NO_3^-. The function of OVs was revealed by computational studies in NRA. Online differential electrochemical mass spectrom-

* Corresponding authors.
E-mail addresses: hu-xj@mail.tsinghua.edu.cn (X. Hu), yingwang@tongji.edu.cn (Y. Wang).

https://doi.org/10.1016/j.cclet.2022.107862
1001-8417/

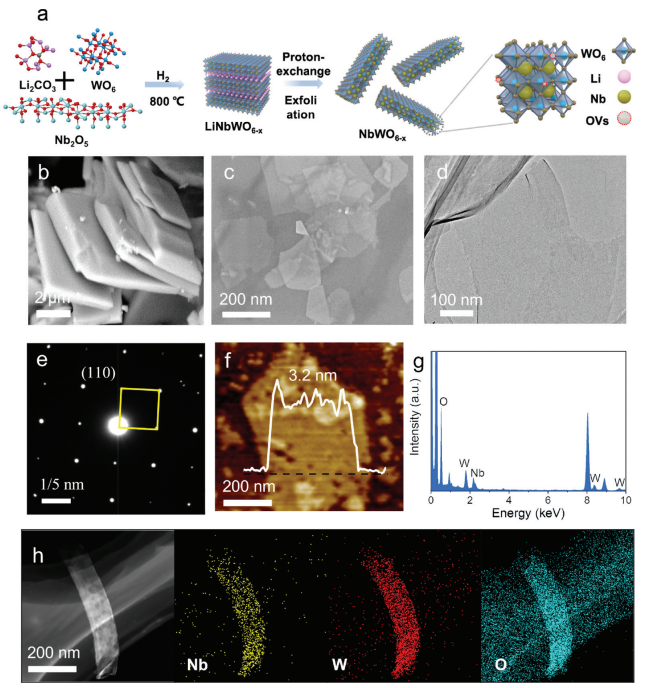

Fig. 1. Morphology and structural analyses. (a) Schematic illustration of the $NbWO_{6-x}$ nanosheets synthesis. SEM images of the (b) $LiNbWO_{6-x}$, (c) $NbWO_{6-x}$. (d) AFM image, (e) TEM image, (f) the SAED pattern, (g) EDS spectrum of the $NbWO_{6-x}$ nanosheets. (h) The HAADF–STEM image and corresponding elemental mapping of Nb, W and O of the $NbWO_{6-x}$ nanosheets.

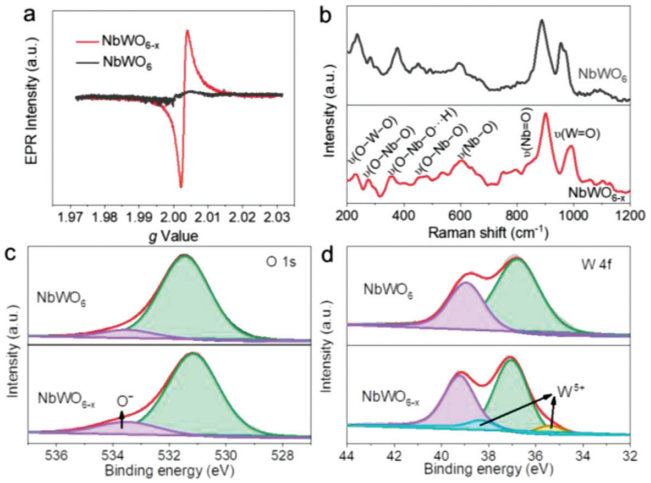

Fig. 2. (a) EPR, (b) Raman spectra, (c) O 1s XPS and (d) W 4f XPS of $NbWO_6$ and $NbWO_{6-x}$.

etry (DEMS) deduced the pathway of NRA involving the O atom in NO_3^- filled in OVs of $NbWO_{6-x}$. This work proved the enhanced function of OVs in NRA, providing a novel strategy for selective NH_3 generation.

The $NbWO_{6-x}$ nanosheets were synthesized *via* thermal treatment and exfoliation (Fig. 1a). Specifically, $LiNbWO_{6-x}$ was synthesized by H_2 atmosphere at 800 °C calcination, and the typical layered nanostructure is observed by scanning electron microscopy (SEM) (Fig. 1b). Then, as-obtained $NbWO_{6-x}$ was prepared by proton-exchange in nitric acid (Fig. S1 in Supporting information) and followed by exfoliation in tetrabutylammonium solution. The few-layer $NbWO_{6-x}$ nanosheets was identified by SEM suggesting the successful exfoliation from layered sample (Fig. 1c). The X-ray powder diffraction (XRD) was performed to determine the crystal phase of $LiNbWO_{6-x}$ and $NbWO_{6-x}$. XRD pattern of the $LiNbWO_{6-x}$ showed the typical diffraction peaks at 9.51°, 19.16°, and 28.64° corresponding to the (001), (002) and (003) crystal planes, respectively (PDF #41–0377/0378) (Fig. S2 in Supporting information) [19,20]. While, $NbWO_{6-x}$ nanosheets revealed (110) crystal planes. The thickness of the nanosheets detected by atomic force microscopy (AFM) is around 3.2 nm, implying the formation of $NbWO_{6-x}$ few layers (Fig. 1d). A transmission electron microscopy (TEM) image revealed an ultrathin sheet-like morphology (Fig. 1e). A high-resolution TEM (HRTEM) image verified distinct lattice fringes corresponding to the (110) lattice planes of $NbWO_{6-x}$ (Fig. S3 in Supporting information) and further confirmed by selected area electron diffraction (SAED) pattern (Fig. 1f). Nb, W and O were distributed homogeneously in the nanosheets manifested *via* energy-dispersive X-ray spectroscopy (EDS) elemental mapping (Figs. 1g and h). For $NbWO_{6-x}$, the characterization data show that the presence of OVs hardly change the morphology.

To further confirm the existence of more OVs in $NbWO_{6-x}$, $NbWO_{6-x}$ was further examined by electron paramagnetic resonance (EPR). $NbWO_{6-x}$ shows a symmetry signal in $g = 2.004$ (Fig. 2a), indicating the presence of electron trapped OVs [21]. While, the Raman peaks of $NbWO_{6-x}$ nanosheets displayed broadening and shifted toward higher wavenumber, further yielding the information of OVs in $NbWO_{6-x}$ (Fig. 2b) [22]. X-ray photoelectron spectroscopy (XPS) is performed to further confirm the existence of more OVs in $NbWO_{6-x}$. The Nb (Fig. S4 in Supporting information), W, and O are detected in the full XPS survey of $NbWO_{6-x}$ and $NbWO_6$ (Fig. S5 in Supporting information). The O 1s XPS spectra show there are two peaks at 531.4 eV (lattice oxygen) and 533.5 eV (OVs) (Fig. 2c). After H_2 treatment, the area ratio of O^-/O_{sum} increases from ~9.6% ($NbWO_6$) to ~18.2% ($NbWO_{6-x}$). Moreover, W 4f XPS spectra show two predominant peaks with binding energy values at 36.9 and 39.1 eV, assigned to $4f_{7/2}$ and $4f_{5/2}$ of W^{6+}, respectively (Fig. 2d). Notedly, only weak peaks originating from W^{5+} appeared in $NbWO_{6-x}$, which proved that more OVs existed in $NbWO_{6-x}$ derived from W-Site consisting with Raman and EPR results [23]. XRD patterns revealed that the diffraction peaks of as-synthesized $NbWO_{6-x}$ are well coincident with $NbWO_6$ (Fig. S6 in Supporting information). In brief, H_2 treatment at 800 °C can create more OVs to generate $NbWO_{6-x}$ with the maintaining of initial few-layer nanosheets morphology and crystal structure.

Electrocatalytic NRA of $NbWO_{6-x}$ is executed using an H-type electrolytic cell. The linear sweep voltammetry (LSV) curves of $NbWO_6$ (Fig. S7a in Supporting information) and $NbWO_{6-x}$ (Fig. S7b in Supporting information) both showed the obvious current density increase in the presence of NO_3^-. $NbWO_{6-x}$ exhibited higher current density compared with $NbWO_6$ during NRA (Fig. S8 in Supporting information). Different applied potentials from −0.3 V to −0.8 V were applied to investigate the NRA performance of $NbWO_{6-x}$ with $NbWO_6$ as comparison (Figs. 3a and b). The variations of NH_3 yield rates (0.021 to 0.068 mmol h^{-1} $mg_{cat.}^{-1}$) and Faradaic efficiency (28.6% to 85.7%) of $NbWO_{6-x}$ were higher than those of $NbWO_6$ (0.019 to 0.049 mmol h^{-1} $mg_{cat.}^{-1}$ and 25.5% to 63.3%), when the potential shifted from −0.3 V to −0.7 V, indicating the high intrinsic activity of $NbWO_{6-x}$. Nevertheless, when the applied potential was further reduced to −0.8 V, it was observed that NH_3 yield rates and Faradaic efficiency were greatly reduced. This phenomenon can be ascribed to the occurrence of excessive HER side reaction [24]. Fig. 3c recorded the typical online DEMS results of $NbWO_{6-x}$ under −0.7 V in 0.10 mol/L Na_2SO_4. The intensity of the *m/z* signal at 17 (NH_3) varied with the applied voltage, and the highest value was achieved at −0.7 V. Meanwhile, weaker NH_3-related signal could be detected when $NbWO_6$ was used as the cathode, in good accordance with the NRA experimental results (Fig. 3d). Moreover, the NO_3^- conversion rate and NH_3 selectivity (97.9%, 86.8%) of $NbWO_{6-x}$ were higher than those

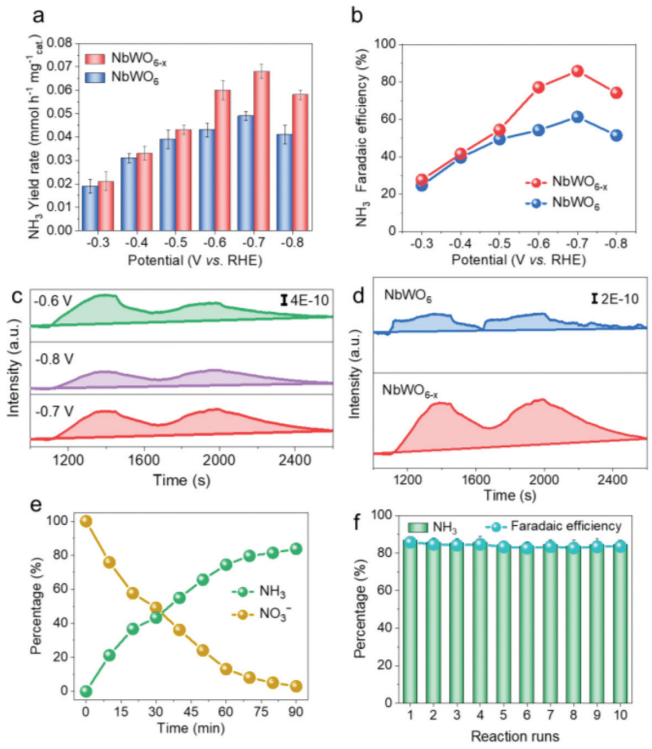

Fig. 3. The NRA performance on $NbWO_6$ and $NbWO_{6-x}$. Potential-dependent (a) NH_3 yield rates and (b) Faradaic efficiency over $NbWO_6$ and $NbWO_{6-x}$. Online DEMS investigations of the signal ($m/z = 17$) (c) at different reaction potentials and (d) over $NbWO_6$ and $NbWO_{6-x}$. (e) Time-dependent concentration change of NO_3^- and NH_3, (f) The consecutive recycling tests over $NbWO_{6-x}$. (7.14 mmol/L of NO_3^-, 0.1 mol/L Na_2SO_4).

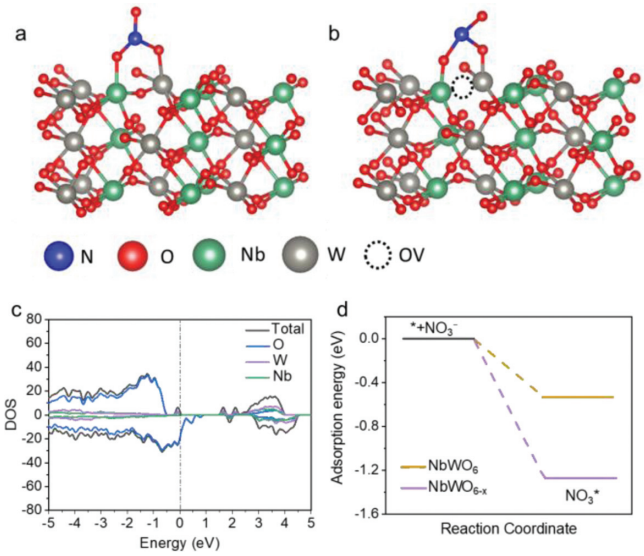

Fig. 4. NO_3^- adsorption models of (a) $NbWO_6$ and (b) $NbWO_{6-x}$. (c) The density of states (DOS) diagram of $NbWO_{6-x}$ and (d) calculated adsorption energies of NO_3^- on $NbWO_6$ and $NbWO_{6-x}$.

of $NbWO_6$ (78.1%, 68.5%) (Fig. S9 in Supporting information). The concentration of NO_3^- continuously decreased while NH_3 concentration was constantly increasing as the reaction time lengthened (Fig. 3e). NO_3^- concentration was found to 0.21 mmol/L within 90 min of $NbWO_{6-x}$ which is much lower than that of $NbWO_6$ (Fig. S10 in Supporting information). The NH_3 selectivity Faradaic efficiency and NO_3^- conversion rate retained more than 80% after 10 cycles of NRA on $NbWO_{6-x}$ indicating high stability and long-term durability (Fig. 3f and Fig. S11 in Supporting information). Furthermore, the selectivity of NH_3 remained basically unchanged even though NO_3^- concentration increased to 14.28 mmol/L, revealing the wide application range of the $NbWO_{6-x}$ (Fig. S12 in Supporting information). In addition, the performance of $NbWO_{6-x}$ was comparable with or even better than other previous reported electrocatalysts for NRA (Table S1 in Supporting information) [25–30]. In addition, ^{15}N isotope labeling experiments *via* ^1H NMR spectra were conducted to further confirm the source of NH_3 (Figs. S13a and b in Supporting information). The ^1H NMR spectra of $Na^{15}NO_3$ as N-source after NRA showed typical double peaks in line with the $(^{15}NH_4)_2SO_4$, while ^1H NMR spectra of $Na^{14}NO_3$ as N-source after NRA showed typical three peaks in accordance with the $(^{14}NH_4)_2SO_4$. Taking into account that the peak area of ^1H NMR is related to the NH_3 content, the NH_3 concentration is further measured with the ^1H NMR standard (Figs. S13c and d in Supporting information). The generated $^{15}NH_3$ and $^{14}NH_3$ calculated by ^1H NMR were very close to the results of colorimetric method using Nesslers reagent (Figs. S14a, b and Table S2 in Supporting information). It is proved quantitatively that the generation of NH_3 comes from NO_3^- as well as demonstrated the accuracy of different quantitative methods. The plausible interpretation is that more OVs of $NbWO_{6-x}$ result in more active sites for adsorption and activation of NO_3^-. Therefore, the introduction of OVs in $NbWO_{6-x}$ can not only accelerate electron transfer, but also effectively adsorb and activate NO_3^-, so as to improve the catalytic activity of NRA.

Computational studies are performed to investigate the OVs-enhanced mechanism over $NbWO_{6-x}$. The structural models of $NbWO_6$ and $NbWO_{6-x}$ are shown in Fig. S15 (Supporting information) and the NO_3^- adsorption models are exhibited in Figs. 4a and b. The density of states (DOS) analysis of $NbWO_6$ shows that O, Nb, W are the most contributing to the valence band and conduction band (Fig. S16 in Supporting information). Whereas, DOS proves the conduction band of $NbWO_{6-x}$ has obvious defect energy levels, which can lead to better electron transitions (Fig. 4c). By introducing OVs on the surface, the Fermi level moves into the conduction band minimum due to the occupation of excess 4d electrons of W. This gives rise to the metallic behavior of $NbWO_{6-x}$ and then improves the conductivity, which is beneficial for electrochemical reduction (Fig. S17 in Supporting information). Furthermore, the NO_3^- adsorption energy on $NbWO_{6-x}$ (−1.27 eV) is much lower than that on $NbWO_6$ (−0.53 eV) which is more conducive to NO_3^- adsorption, thus promoting the NRA (Fig. 4d). The mechanism was verified to W cations with their adjacent OVs and specific interacting d orbital electrons of $NbWO_{6-x}$ can serve as unsaturated active centers that strengthen the ability to adsorb/activate NO_3^-, making the NRA more conducive to happening.

DEMS system was used to monitor the volatile intermediates and products deducing the NRA path. When the applied voltages were varied from −0.3 V to −0.9 V, signals at *m/z* values of 46, 30, 33 and 17 (corresponding to NO_2, NO, NH_2OH and NH_3, respectively) appeared during continuous cycles (Fig. 5a). Thus, the reaction pathway of NRA could be deduced: $NO_3^- \rightarrow NO_2^- \rightarrow NO \rightarrow NH_2OH \rightarrow NH_3$. Figuratively, the possible reaction pathway for NRA on the $NbWO_{6-x}$ with OVs is proposed and illustrated in Fig. 5b (labeling three O atoms in NO_3^- as O^1, O^2, and O^3, respectively). In this pathway, NO_3^- adsorption on $NbWO_{6-x}$ surface with OVs to form NO_3^*. The next reduction reaction by proton-electron pair will take O^3 in NO_3^* and the two-H away to form NO_2^* and H_2O^3. Next, O^2 will then be released by the second hydrogenation step to form NO^* and H_2O^2. Subsequently, three proton-electron pairs couple with NO^* to form NH_2OH^*, leaving O^1 on the OV site. Finally, O^1 will be reduced by two protons to form H_2O^1 and NH_3, recovering the OVs on the surface. Above all, OVs of $NbWO_{6-x}$ can make the N–O bond weaken *via* filling

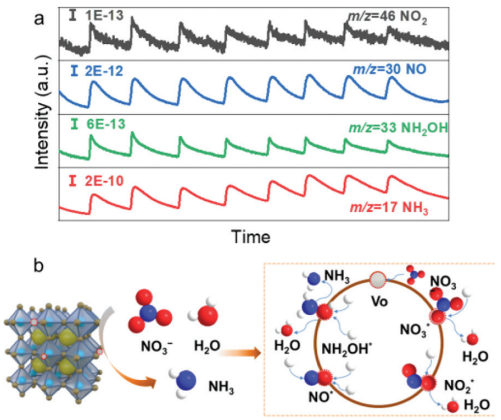

Fig. 5. Proposed reaction pathways for the NRA on $NbWO_{6-x}$. (a) DEMS measurements of $NbWO_{6-x}$. (b) Possible reaction pathways of NRA on the $NbWO_{6-x}$ with OVs. The red dashed circles represent OVs.

with O of NO_3^- and hinder the undesirable byproducts consisting with the experimental results.

In summary, $NbWO_{6-x}$ nanosheets with OVs were successfully prepared for enhancing the electrocatalytic NRA activity. $NbWO_{6-x}$ nanosheets with OVs exhibited the high activity and excellent durability toward NRA. Experimental data and computational studies revealed OVs were beneficial to electron transitions and lower NO_3^- adsorption as well activation energy. DEMS measurements were introduced to detect the production of NO and NH_2OH during the NRA which demonstrated the reaction mechanism and pathway. This work will provide new insight for constructing OVs in perovskite oxides as efficient electrocatalysts toward NRA.

Declaration of competing interest

The authors declare that they have no known competing financial interests or personal relationships that could have appeared to influence the work reported in this paper.

Acknowledgments

The authors appreciate the supports from the National Natural Science Foundation of China (NSFC, Nos. 22074104 and 51978491), National Program for Support of Top-notch Young Professionals, the Fundamental Research Funds for the Central Universities (No. 2022-4-ZD-07), “Shuguang Scholar Program” (No. 17SG52) by Shanghai Education Development Foundation and Shanghai Municipal Education Commission, Liaoning Provincial Natural Science Fund Project (No. 2019-ZD-0550), and Scientific Research Foundation of Shanghai Institute of Technology (No. YJ2021-24).

Supplementary materials

Supplementary material associated with this article can be found, in the online version, at doi:10.1016/j.cclet.2022.107862.

References

[1] D. Yao, C. Tang, L. Li, et al., Adv. Energy Mater. 10 (2020) 2001289.
[2] J. Wang, T. Feng, J. Chen, et al., Nano Energy 86 (2021) 106088.
[3] M. Kitano, S. Kanbara, Y. Inoue, et al., Nat. Commun. 6 (2015) 6731–6739.
[4] D. Bao, Q. Zhang, F.L. Meng, et al., Adv. Mater. 29 (2017) 1604799.
[5] J. Wang, L. Ling, Z. Deng, W.X. Zhang, Sci. Bull. 65 (2020) 926–933.
[6] V. Rosca, M. Duca, M.T.d. Groot, M.T.M. Koper, Chem. Rev. 109 (2009) 2209–2244.
[7] D.E. Canfield, A.N. Glazer, P.G. Falkowski, Science 330 (2010) 192–196.
[8] T. Feng, J. Wang, Y. Wang, et al., Chem. Eng. J. 433 (2022) 133495.
[9] F. Ni, Y. Ma, J. Chen, W. Luo, J. Yang, Chin. Chem. Lett. 32 (2021) 2073–2078.
[10] H.O. Song, Y. Zhou, A.M. Li, S. Mueller, Chin. Chem. Lett. 23 (2012) 603–606.
[11] N. Barrabés, J. Sá, Appl. Catal. B 104 (2011) 1–5.
[12] R. Jia, Y. Wang, C. Wang, et al., ACS Catal. 10 (2020) 3533–3540.
[13] J. Wang, T. Feng, J. Chen, J.H. He, X. Fang, Research 2022 (2022) 9837012.
[14] D. Guo, S. You, F. Li, Y. Liu, Chin. Chem. Lett. 33 (2022) 1–10.
[15] Y. Ren, Y. Liu, F. Liu, et al., Chin. Chem. Lett. 32 (2021) 2519–2523.
[16] W. Zheng, Y. Liu, W. Liu, et al., Water Res. 194 (2021) 116961.
[17] Z. Sun, R. Huo, C. Choi, et al., Nano Energy 62 (2019) 869–875.
[18] K. Chu, F. Liu, J. Zhu, et al., Adv. Energy Mater. 11 (2021) 2003799.
[19] Y. Liu, J. Xiong, S. Luo, et al., Chem. Commun. 51 (2015) 15125–15128.
[20] J. Wang, Y. Ren, H. Liu, et al., Adv. Mater. 34 (2021) e2104958.
[21] N. Zhang, X. Li, H. Ye, et al., J. Am. Chem. Soc. 138 (2016) 8928–8935.
[22] T. Zheng, W. Sang, Z. He, et al., Nano Lett. 17 (2017) 7968–7973.
[23] N. Zhang, X. Li, Y. Liu, et al., Small 13 (2017) 1701354.
[24] H. Xu, J. Wu, W. Luo, et al., Small 16 (2020) e2001775.
[25] L. Wang, M. Li, C. Feng, et al., J. Electroanal. Chem. 773 (2016) 13–21.
[26] C. Li, K. Li, C. Chen, et al., Sep. Purif. Technol. 237 (2020) 116485.
[27] L. Mattarozzi, S. Cattarin, N. Comisso, et al., Electrochim. Acta 89 (2013) 488–496.
[28] D. Yin, Y. Liu, P. Song, et al., Electrochim. Acta 324 (2019) 134846.
[29] M. Chen, H. Wang, Y. Zhao, et al., Nanoscale 10 (2018) 19023–19030.
[30] W. Li, C. Xiao, Y. Zhao, et al., Catal. Lett. 146 (2016) 2585–2595.